Revealing the defect-dominated oxygen evolution activity of hematene

Bishnupad, M.; Wei, Y.; Ghorbani Asl, M.; Krasheninnikov, A.; Parasmani, R.; Bikash, K. J.;

Originally published:

March 2020

Journal of Materials Chemistry A 8(2020)14, 6709-6716

DOI: https://doi.org/10.1039/D0TA00422G

Journal of
Materials Chemistry A

Materials for energy and sustainability

Accepted Manuscript

This article can be cited before page numbers have been issued, to do this please use: B. Mohanty, Y. Wei, M. Ghorbani-Asl, A. V. Krasheninnikov, P. Rajput and B. K. Jena, *J. Mater. Chem. A*, 2020, DOI: 10.1039/D0TA00422G.

ROYAL SOCIETY OF CHEMISTRY

rsc.li/materials-a

View Article Online
DOI: 10.1039/D0TA00422G

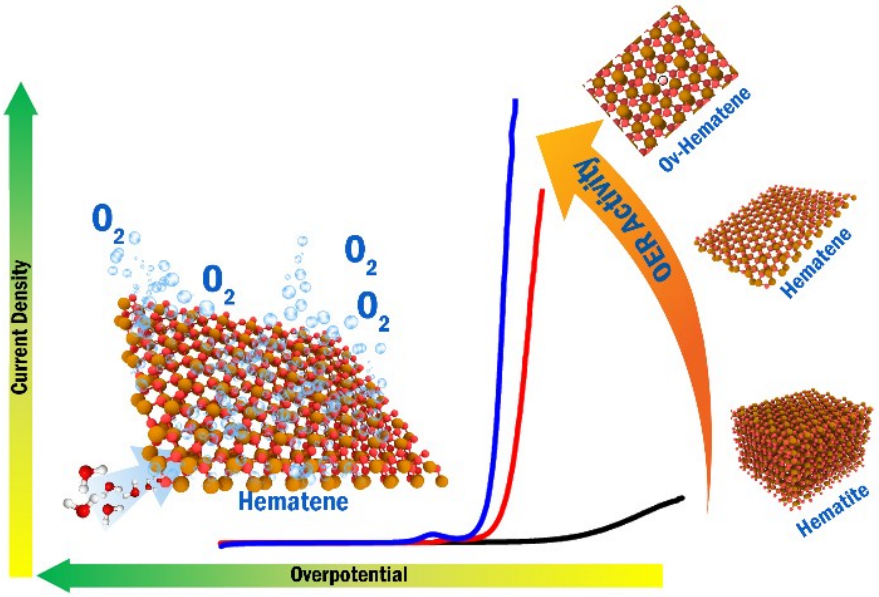

View Article Online
DOI: 10.1039/D0TA00422G

COMMUNICATION

Revealing the defect-dominated oxygen evolution activity of hematene

Received 00th January 20xx,
Accepted 00th January 20xx

DOI: 10.1039/x0xx00000x

Bishnupad Mohanty,[a] Yidan Wei,[c] Mahdi Ghorbani-Asl,[c] Arkady V. Krasheninnikov,[c,d*] Parasmani Rajput,[e] Bikash Kumar Jena[a,b*]

Abstract

Oxygen electrocatalysis is vital for advanced energy technologies, but inordinate challenges remain due to the lack of highly active earth-abundant catalysts. Herein, by nanostructuring and defect engineering, we enhance the catalytic properties of naturally occurring, but normally inactive ore hematite (Ht) by converting it to hematene (Hm) with oxygen vacancies (Ov-Hm), that becomes an efficient oxygen evolution reaction (OER) catalyst, being even superior to the state-of-the-art catalyst IrO_2/C, with a current density of 10 mA/cm^2 at a lower overpotential of 250 mV. The first-principles calculations reveal that the reduced dimensionality and defects on the Hm surface locally modify the charge around the adsorption sites, which results in a reduction of the potential barrier in the OER process. Our experimental and theoretical insights suggest a promising route to the development of a highly active electrocatalyst from the naturally occurring and abundant material for OER applications.

Introduction

The ever-growing energy crises and environmental issues are the major threats for human society, which has been a stimulus to the exploration of clean and renewable energy conversion and storage technologies.[1,2] Among these, electrochemical water splitting is a promising approach to fulfill the worldwide energy requirements.[3,4,5] However, the efficiency of this technology is restricted due to the sluggish kinetics of the anodic oxygen evolution reaction (OER) owing to the multistep four-electron oxidation process.[6,7] As a result, low cost, earth-abundant, and highly efficient catalysts are required to improve overall energy efficiency. To date, Ir- and Ru-based materials are still recognized as the benchmark catalysts owing to their superior activity.[8,9] However, the high cost and scarcity of these noble metals have limited their widespread applications. Therefore, earth-abundant efficient electrocatalysts should be designed for OER. In that context, transition metal ores including Ni, Co, Fe, Mo, etc. have been extensively explored.[10–15] However, most of the catalysts have modest electrocatalytic performance due to their poor electrical conductivity, a limited number of active sites, and low adsorption energy of the reactants. So, for tuning their electrochemical performance, various optimizing protocols such as synthesis of ultrathin two-dimensional (2D) materials, creating defects, forming the composite, doping by foreign atoms, etc. have been studied.[16–21] As a result of these efforts, these catalysts demonstrated a higher catalytic activity, being even better than the benchmark catalysts.[15,16] So, applying these strategies to naturally occurring ore and utilizing it in electrochemical applications should be quite beneficial as well as cost-effective, but it also presents a significant challenge.

Among these strategies, the development of ultrathin 2D nanostructured materials and defect engineering have recently received particular attention.[16,22,23] 2D materials possess a unique structure, atomic-scale thickness, high surface-to-volume ratio, exhibit quantum size effect and unusual physical, chemical, and electronic properties. Very recently, a new class of non-vdW 2D materials including hematene and ilmenene have been successfully exfoliated from their non-layered crystal counterparts.[24,25] In contrary to typical 2D materials, the rich unsaturated coordination sites in these nanomaterials provide excellent opportunities for modulation of their properties as well as new functionalities for various applications.

Among the Fe-based catalysts, hematite (α-Fe_2O_3) is the most promising material for photochemical and photoelectrochemical applications.[26,27] At the same time, it is ineffective in electrochemical applications due to its low electrical conductivity and low concentration of active sites. However, its earth-abundance and low cost in comparison with other catalysts motivate the efforts aimed at improving its electrocatalytic activity. Herein, we synthesize crystalline hematene (Hm) from natural hematite (Ht) by liquid exfoliation. Using a chemical reduction method, oxygen vacancies are created in Hm for exploring its electrochemical OER activity. The as-prepared Hm with oxygen vacancies (Ov-Hm) demonstrates a

[a] CSIR-Institute of Minerals and Materials Technology, Bhubaneswar-751013, India.
[b] Academy of Scientific & Innovative Research (AcSIR), Ghaziabad- 201002, India.
[c] Helmholtz-Zentrum Dresden-Rossendorf, Institute of Ion Beam Physics and Materials Research, 01328 Dresden, Germany
[d] Department of Applied Physics, Aalto University School of Science, PO Box 11100, 00076 Aalto, Finland
[e] Atomic & Molecular Physics Division, Bhabha Atomic Research Centre, Trombay, Mumbai-400085, India
[f] *email: bikash@immt.res.in, a.krasheninnikov@hzdr.de, mahdi.ghorbani@hzdr.de.

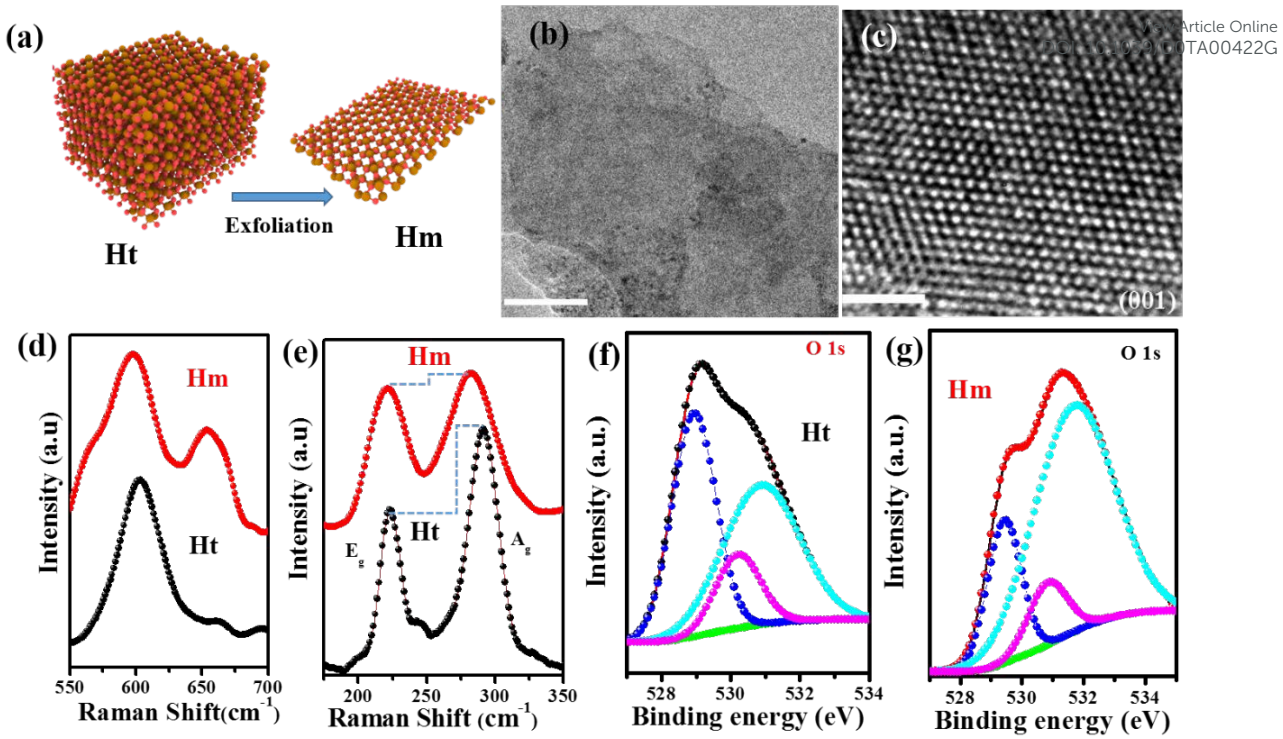

Fig.1 Structural characterizations of as-synthesized Hematene (Hm) catalysts. (a) Scheme showing the exfoliation of Ht to Hm. (b) TEM (scale bar: 100 nm) and (c) HRTEM image of ultrathin Hm (scale bar:2 nm). (d) Formation of Eu mode in the Raman spectra of Hm. (e) Change in intensity of ratio of E_g to A_g mode. XPS spectra of O 1s for Ht (f) and Hm (g).

remarkable activity and stability as a catalyst for OER under alkaline conditions. The first-principles calculations provide microscopic insights into the experimental observations of the enhanced catalytic performance of Ov-Hm, which is attributed to the modification of the electronic charges on the active sites and adsorption energy of the OER intermediates in the presence of oxygen vacancies.

Results and discussion

2.1 Synthesis and characterization of Hm. Few-layers of Hm were synthesized via liquid exfoliation from Ht (Figure 1a). The The morphology of Hm is supported by high-resolution transmission electron microscopy (HRTEM) analysis (Figure 1b, c). The HRTEM reveals the (001) plane of Hm (Figure 1c).[24] The selected area electron diffraction (SAED) pattern confirms the single-crystalline nature of the 2D sheets.[28] The estimated thickness of as-synthesized Hm supports the formation of bi/trilayers of sheets (Figure S1). The X-ray diffraction (XRD) was used to study the crystalline structure of Ht and Hm (Figure S2a). The XRD patterns clearly show the crystal structure of α-Fe_2O_3 without any impurities. The XRD pattern of Hm is perfectly indexed with Ht. Also, in comparison to Ht, the main peak is shifted to a higher angle with uniform broadening, which may be attributed to the strain present in the sample (Figure S2b).[24,29] In the Raman spectra of Ht, six dominated peaks are observed (Figure S3),[30,31] while seven dominated peaks are formed in the case of Hm. The additional peak appeared at 659 cm^{-1} is assigned to the Eu modes, and it indicates the structural disorder within the crystal lattice (Figure 1d).[24] In addition, the intensity and frequencies of the dominant A_{1g} and E_g modes are changed in Hm (Figure 1e). The A_{1g} modes shift towards lower frequencies (redshifted), whereas the E_g modes appear at higher frequencies (blue shifted). All the above results are in a very good agreement with the previous experimental data[24] supporting the successful preparation of Hm. The X-ray photoelectron spectroscopy (XPS) spectra of Ht and Hm are shown in the Figure S4a. Fe 2p spectrum shows the characteristic peaks of Ht, but a shift of the peaks to higher binding energy was observed in Hm as compared to Ht (Figure S4b). The O 1s spectrum of Ht and Hm displays two peaks centered at 529.5 eV and 531.5 eV corresponding to the lattice oxygen and undercoordinated surface oxygen atoms, respectively (Figure 1f and 1g). The spectrum shows an increase in the intensity of the latter for Hm (Figure S4c) that signifies the increase in the number of surface oxygen atoms due to the 2D morphology of Hm.[24,25,28]

2.2 Synthesis and characterization of Ov-Hm. Further, we have created oxygen vacancies on the surface of Hm by adopting a chemical reduction method. [28,32] The reducing agent provides electrons to the metal ions (Fe^{+3}) as a result of the reduction in the oxidation state of metal ions (Fe^{+2}). To maintain the charge neutrality, oxygen vacancies appear (Figure 2a).[33] The Raman peaks of Ov-Hm are well indexed with the characteristic peaks of Hm (Figure S5). The negative shifting and broadening of the peaks point out the oxygen deficiency in Ov-Hm (Figure S5b).[34] In XPS of Fe 2p spectrum, in addition to the satellite peak of Fe^{+3} (719.5 eV), another small peak appears at 715.8 eV that indicates the presence of Fe^{2+} (Figure 2b).[35]The formation of oxygen vacancies on the surface of Ov-Hm is balanced by the conversion of some Fe^{3+} species to Fe^{2+}. The analysis of O 1s spectrum also reveals the presence of oxygen vacancies on the surface of Hm (Figure 2c).[34] The peak at 531.5 eV has a higher intensity in comparison to Hm which suggests an

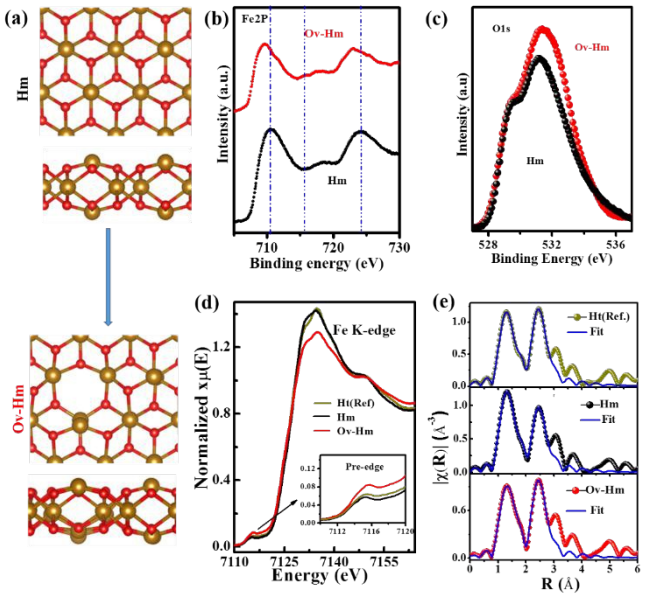

Fig.2 Structural characterizations of as-synthesized Ov-Hematene (Ov-Hm) catalysts. (a) Schematic presentation of the transformation from Hm to Ov-Hm. Brown spheres represent Fe atoms and red spheres stand for O. (b) Enlarged Raman spectra showing the down shift of the peaks after vacancy creation. (c) Core-level Fe 2p XPS spectra overlap of Hm and Ov-Hm. (d) Normalized Fe K-edge XANES spectra of all samples. (e) Fe K-edge Fourier transform of k2-weighted of all thin films. The symbol shows data and solid lines are the best fitting data.

increase in the concentration undercoordinated surface oxygen atoms in the matrix of Hm.[34,36] The Mott–Schottky (M-S) analysis is another effective method for confirming the presence of oxygen vacancies.[34] The donor density (N_d) was calculated from capacitance measurements at 10 kHz frequency (Equation S12). The N_d values for Hm and Ov-Hm are estimated to be 4.06×10^{18} and 3.61×10^{19}, respectively (Figure S6). As dopant is not used in the present case, the increase in donor density attributes to the oxygen vacancies.[34,35] To understand the local bonding environment of Fe, Fe K-edge XANES spectra were carried out (Figure 2 (d)). The decrease in the intensity of the pre-edge peak of Hm around 7115 eV suggests a higher local oxygen coordination environment around the Fe atoms. Further increase in the intensity of the pre-edge peak of Ov-Hm suggests reduced oxygen coordination.[28,37] The corresponding Fourier transform (FT) of Fe edge XAFS spectra of all samples were fitted using a Hematite R-3c crystal structure (Figure 2e) and summarised in Table S1. The FT data clearly shows that the Hm has increased coordination number due to an increase in the number of surface oxygen atoms.[37] Further, the coordination number of Fe decreased in Ov-Hm that suggests a higher concentration of oxygen vacancies in Ov-Hm.

2.3 Electrocatalytic activity evaluation. The 2D nature of Hm associated with a high surface area suggests that the material can be electrocatalytically active towards OER. Besides, structural defect engineering is known to enhance the activity of 2D materials for various electrocatalytic reactions. In the case of OER on metal oxides, the catalytic activity depends on two major factors: the number of active sites subjected to electrolyte and the oxidation state of the transition metal. Therefore, defects such as vacancies have a remarkable influence on the adsorption-desorption efficiency of the OER intermediates and further improve the electrocatalytic performance.[17,23] Figure 3a presents the LSV polarization plots of the as-synthesized materials. The LSV plots are presented in RHE scale after calibration of the Ag/AgCl reference electrode in 1M KOH (Figure S7) and also before and after iR correction (Figure S8). The modified Hm electrode efficiently catalyses the OER activity with increased current density (~100 times) and lower onset-overpotential (180 mV) as compared to Ht. The OER activity of Hm is further enhanced by creating defects on the surface. To yield a current density of 10 $mAcm^{-2}$, a lower overpotential (250 mV) is required for Ov-Hm in comparison to Hm (280 mV). In addition, Ht does not achieve the yield values of 10 $mAcm^{-2}$, which signifies the importance of the reduced dimensionality in the activity of Hm. The OER activity of Ov-Hm shows a noticeable improvement over the state-of-the-art catalyst IrO_2/C (Figure 3b). To study the reaction kinetics of the aforementioned catalysts, the Tafel plots were analyzed (Figure 3c). The Ov-Hm shows the lowest Tafel slope value of 34 mV/dec among the studied samples e.g. two times faster reaction kinetics as to IrO_2/C. Furthermore, the OER activity of Ov-Hm is compared to other Fe based catalysts and stands as the best Fe-based OER catalysts to our knowledge (Table S2).

For optimizing the concentration of oxygen vacancies in Hm, the OER activity has been summarized at different periods of the reduction reaction (Figure S9 a, b and discussion in SI). During the OER polarization, the pre-oxidation peak of Fe was observed for Hm and Ov-Hm, but not in Ht. That plays a crucial role in the formation of active oxyhydroxide on the surface and shows the importance of defects as active sites for OER.[38,39] It is assumed that the increase in the concentration of oxygen vacancy on the surface of the catalysts facilitates the formation of oxyhydroxide. Cyclic voltammetry (CV) has been carried out to understand the significance of the observed OER pre-oxidation peak (Figure S10 a, b). Such a redox peak is observed for Hm and Ov-Hm, but not for Ht. This suggests that the surfaces of Hm and Ov-Hm undergo an irreversible surface reconstruction and form a suitable OER catalytic surface. Additionally, oxygen vacancies provide structural flexibility in the catalysts for surface reconstructions.

On the electrocatalysis surfaces, OER proceeds through consecutive four steps proton-coupled electron transfer mechanism and metal centers mostly act as active sites. On metal oxides surfaces, active metal centers as well as surface oxygen act as active sites. Previous studies showed that the involvement of oxygen on metal oxide surfaces in the OER mechanism was dependent on the pH value.[40,41] The pH-dependent activity of Ov-Hm, Hm and Ht (Figure S11 a-c) confirm that the involvement of undercoordinated surface oxygen atoms is crucial for controlling the OER process. The pH dependency arises due to the change in the affinity of hydroxide ions and electron transfer kinetics at the catalysts-electrolyte interface. The change in current density is higher in Ov-Hm than Hm or Ht (Figure S11 d). To track the undercoordinated surface oxygen atoms, a chemical probe tetramethylammonium cation (TMA^+) is

View Article Online
DOI: 10.1039/D0TA00422G

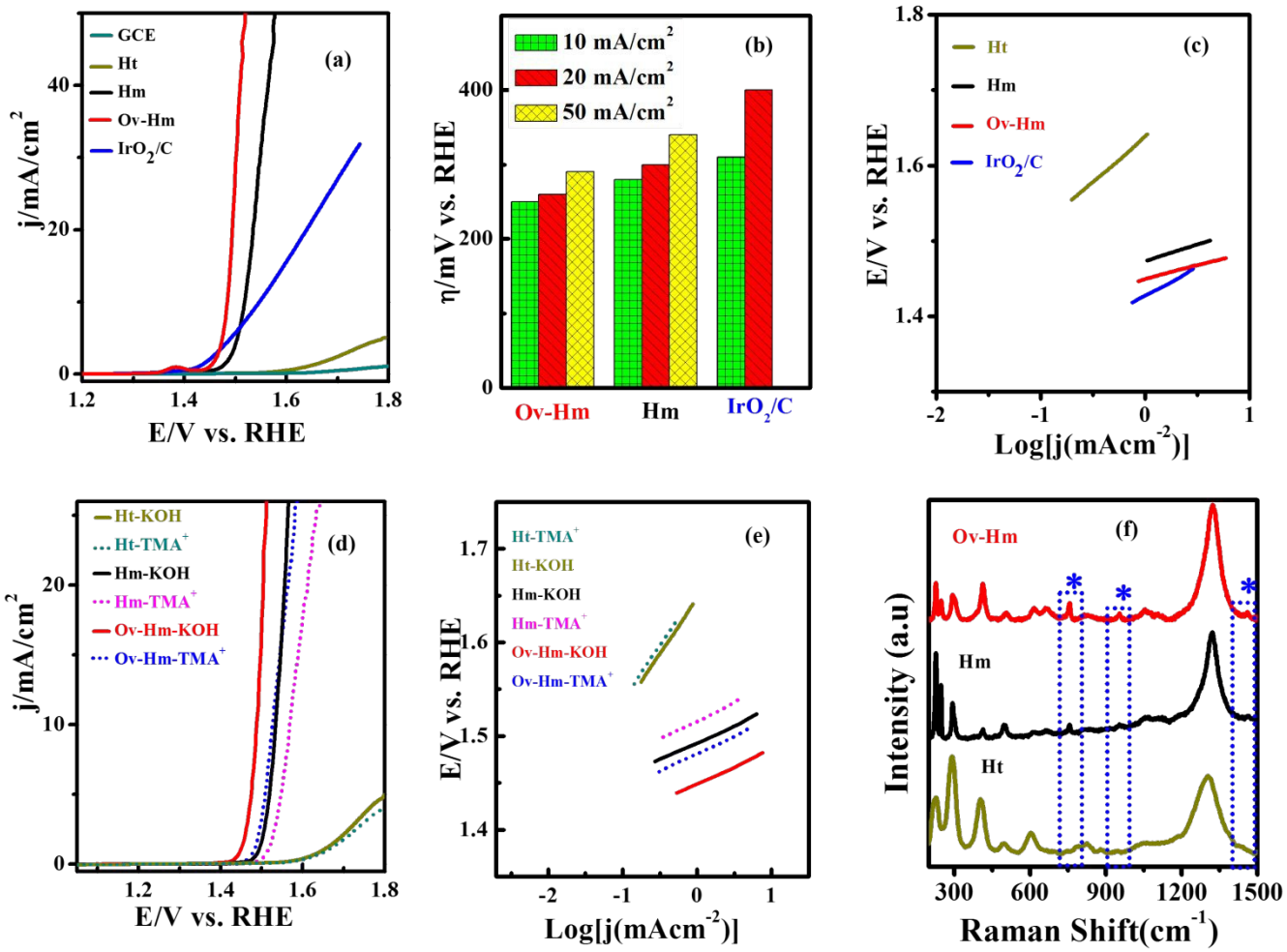

Fig.3 Electrocatalytic OER performance of Hm and Ov-Hm. (a) LSV polarization plot of Ov-Hm, Hm, Ht, IrO_2/C, and bare GEC, (b) Overpotential comparison of Ov-Hm, Hm and IrO_2/C at a current density of 10, 20 and 50 mA/cm^2. (c) Corresponding Tafel slopes (d) Polarization curves of Ov-Hm, Hm and Ht in 1M KOH and TMAOH. (e) corresponding Tafel slopes. (f) Raman spectra of Ov-Hm, Hm and Ht after treating with 1M TMAOH.

added to the electrolytic solutions due to its specific interaction with surface oxygen.[40,42] The OER activity of Ov-Hm and Hm is dramatically reduced as compared to Ht in the presence of TMA^+ (Figure 3d). Similarly, the Tafel slope of Hm and Ov-Hm is suppressed (Figure 3e). This suggests that TMA^+ ions bind the undercoordinated surface oxygen atoms during the OER so decrease the catalytic activity. The binding of TMA^+ is also confirmed by Raman spectroscopy, where three additional peaks in the spectra appeared at 755, 952 and 1463 cm^{-1} (Figure 3f).[40] Interestingly, the intensity of all the three peaks are higher in Ov-Hm than in Hm albeit no such peaks are observed in Ht. The above results showed that undercoordinated surface oxygen atoms act as active centers for electrocatalytic OER applications.

The formation of oxygen bubbles during the electrocatalytic reaction is confirmed by Rotating Ring-Disk Electrode (RRDE) experiment.[43,16] The exclusive generation of O_2 is supported by the oxygen reduction reaction (ORR) polarization curve collected from the ring electrode at a constant disk potential of 1.5 V (Figure 4a). During OER polarisation, a very negligible current density was

observed in the ring electrode that assigned to the electro-oxidation of generated H_2O_2 (Figure 4b). This observation validates the four-electron pathway for OER on Ov-Hm. The Faradic efficiency was calculated from the ratio of ring and disc current during the RRDE experiment (Equation S13) to evaluate the performance of the catalyst.[16,43] By applying 300 µA constant current on the disk electrode, 58.7 µA current was generated at the ring electrode during OER (Figure 4c). This corresponds to a high Faradic efficiency of 97.8% for Ov-Hm. The enhanced OER activity of the as-synthesized catalysts was further accessed by electrochemical surface area (ECSA, Figure S12), roughness factor (R_f), turnover frequency (TOF), mass activity (MA) and the results are summarised in Figure 4d and Table S3. The higher ECSA, TOF and MA value of Ov-Hm suggest higher intrinsic activity compared to other catalysts (The details are discussed in SI).

alkaline medium by M-S analysis (Figure S14 and discussion in SI). The linear fit of the M-S plot gives the positive slopes that indicate the materials are n-type semiconductors (Figure S15). The flat band potential (V_{fb}), donor density (N_d) and Debye radius (L_D) are derived from M-S plot (Equations S11, S12, S13 and Table S4). The high value of V_{fb} and low N_d observed for Ht suggest its unsuitability for photocatalytic and electrocatalytic activity. Among the considered catalysts, Ov-Hm shows the highest negative V_{fb}, highest N_d and lowest L_D value that signifies the increased electron density and charge-transfer ability toward efficient OER process. Ov-Hm also shows excellent stability towards OER (Figure S16a). After 5,000 cycles of continuous operation, slight potential degradation was observed. Similarly, in chronopotentiometry test, Ov-Hm exhibited a very steady potentiometric profile with 99% operational potential retention over 30 h of continuous operation whereas the benchmark catalysts IrO_2/C yields 95% operational potential retention over only

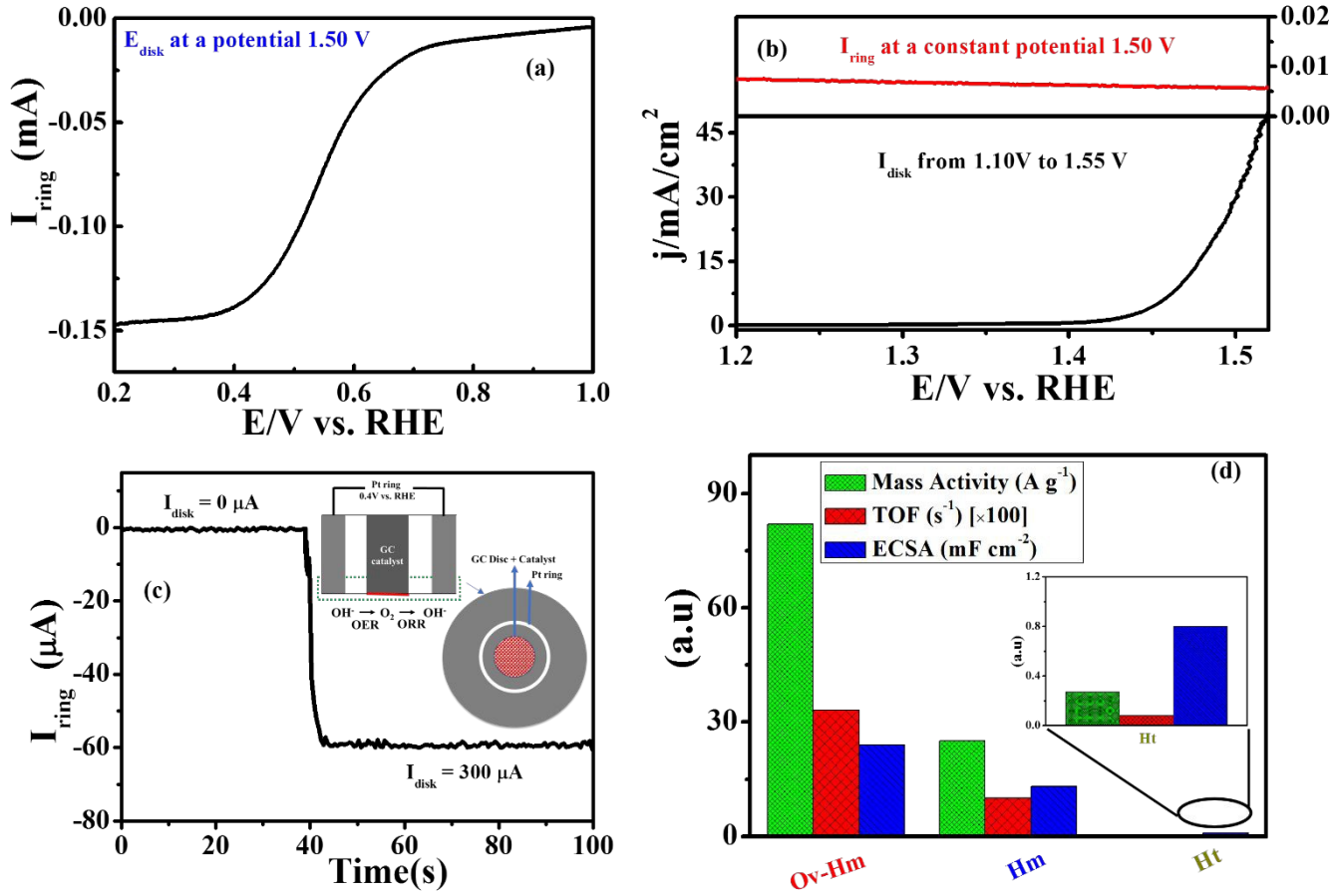

Fig.4 RRDE experimental and electrochemical characterization of Hm and Ov-Hm. (a) LSV curve of ORR at a disc potential of 1.50 V (b) RRDE measurement of Ov-Hm in O_2-saturated 1M KOH solution (ring potential: 1.50 V). (c) Faradic efficiency calculation of Ov-Hm by using RRDE technique. The inset illustrates the efficiency testing mechanism and configuration of the RRDE. (d) Comparison plot of mass activity, TOF, and ECSA of Ov-Hm, Hm and Ht.

Electrochemical impedance spectroscopy (EIS) analysis (Figure S13 and Table S3) reveals lower charge transfer resistance in Hm than Ht. The creation of oxygen vacancies further reduces the charge transfer resistance and develops metallic character on Ov-Hm, which increases the OER kinetics. The electrocatalytic properties of the catalysts were explored at the interface of electrolyte-electrode in 9 h electrolysis (Figure S16b). The structural changes in the materials were assessed after the stabilty experiment. The post charactrizations using TEM, XRD and Raman spectroscopy were carried out for Ov-Hm after stability test (figure S17). No significant changes were observed, which suggests the robustness of the catalysts.

View Article Online
DOI: 10.1039/D0TA01323C

2.4 Density Functional Calulations. To rationalize the above experimental observations and assess the effects of reduced thickness and vacancies on the catalytic activity of bulk Ht, Hm and Ov-Hm towards OER, first-principles calculations have been carried out. In the case of Ht, we considered the (001) surface with Fe-termination and the (104) surface terminated with oxygen. As for Hm, a (001) faceted slab was created by isolating directly from its bulk counterpart (see Figure 1) according to the recent experimental report.[24] The same experiment showed that the (001) sheet exhibits higher structural stability than the (010) facet, while the later converts to a significantly distorted configuration after exfoliation. The higher stability of the (001) facet can be attributed to the highest density of broken bonds in the trigonal crystal structure of Hm.[44] In addition, surface coverage may play an important role in the stability of non-vdW 2D samples and further affect the catalytic properties of these materials. In this work, we assumed that the surface is not passivated with reaction intermediates.

The in-plane lattice parameters of monolayer are ~3% larger than that of the bulk counterparts while the thickness is about 3.01 Å, in a good agreement with the experimental value of 3.02 Å.[24] The fully optimized lattice parameters for bulk and monolayer structures are summarized in Table S5. We then evaluated the surface energy of all the studied surfaces. The calculated energy of (001) surface is 1.12 J/m^2 which is lower than that for the (104) surface (1.41 J/m^2) under oxygen-rich conditions, which is consistent with the previous density-functional theory (DFT) results [45]. In addition, the creation of Hm from Ht is associated with a surface energy of 1.03 J/m^2, which is much higher than those for layered materials, e.g. 0.37 J/m^2 for graphene[46] and indicates the non-van der Waals character of Hm layers.

Oxygen vacancies are one of the most common defects in transition metal oxides due to their low formation energies.[47] In order to rationalize the effects of vacancies on OER, we removed one of the oxygen atoms in the outermost layer of the studied systems. In our supercell models with ideal O-termination, one O-vacancy corresponds to a concentration of ~4% for (001) and (104) hematite surfaces, i.e., one O atom removed from the 24 outermost O atoms in the supercell. Our calculations showed that the vacancy formation energy in Hm (1.24 eV) is significantly lower than that on the corresponding bulk surface (3.75 eV), suggesting that oxygen vacancies are energetically more stable in Hm than on the surface of Ht.In Figure 5, we analyze the OER reaction mechanism on Ht and Hm surfaces by presenting the free energy changes (ΔG) of the intermediates and products. The reaction intermediates for surfaces with and without vacancy are plotted in Figure S18-S21. For each intermediate step, the most favorable surface-active site was found by comparing the adsorption energy of various surface sites. Our results show that the limiting step of the OER process on the (001)-Ht is step-I with an overpotential of 1.59 eV, which is similar to the previous report[48] while the overpotential is smaller than surfaces are passivated with oxygen or hydroxyl under acid environment[49,50]. In comparison to the (001) or (104) Ht surfaces (Fig. S22), Hm has a smaller OER overpotential, as evident from step-II in Figure 5 and Table S6. The presence of vacancies further reduces the potential barrier from 1.39 eV to 1.28 eV in Ov-Hm (Table S6). Our results display a decrease in the adsorption energy of the intermediates, which correlates with the local changes in the electronic charge of the adsorption sites induced by the oxygen vacancies. Mulliken population analysis (Table S7) confirms the depletion of the partial charge on the intermediate molecules in the presence of the defect. Our findings are consistent with the recent experimental[51] and theoretical reports[51,52] confirming the positive effect of oxygen vacancy on the catalytic activity of the Ht surface. By applying the overpotential of U_{ext} = 1.28 V, it can be seen that all reaction steps become exothermic for the catalyst with oxygen vacancies. We further studied the effects of dissociated oxygen and we found that the surface coverage affects the local environment of the active sites and can significantly reduce binding energy of *O_2 (See Figure S22).

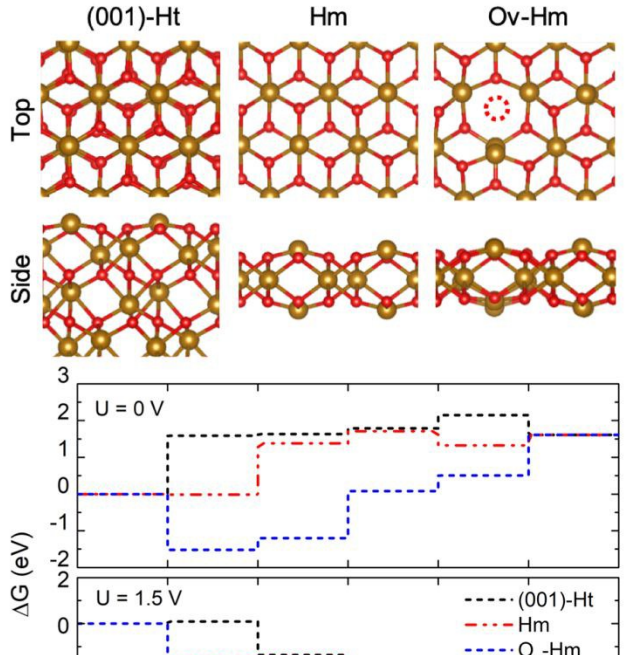

Fig. 5 DFT calculation of Hm and Ov-Hm. Top: The optimized atomic structures of (001)-Ht, Hm and Ov-Hm. Brown spheres represent metal ions and red spheres show oxygen. The dashed black circles indicate the position of oxygen vacancy. Bottom: Free energy profiles for OER on (001)-Ht, Hm and Ov-Hm. The results are obtained at external potential U_{ext} = 0.0, 1.5 V and pH = 14.

Conclusions

In summary, we have demonstrated that both structure and defect engineering help to activate metal oxides for OER and that defective surfaces act as active centers for electrocatalytic OER. The exfoliation of Hm from naturally occurring Ht combined with defect engineering increases the number of active sites involving surface oxygen (in Hm), which not only facilitates the reaction, but also provides structural flexibility and increased conductivity in the catalysts. As a result, Ov-Hm exhibits excellent OER activity and durability in alkaline medium. The catalysts achieve the current density of 10 mA/cm^2 at an overpotential of 250 mV and durability up to 30 hours and 5000 cycles. The role of undercoordinated surface oxygen atoms in the OER mechanism was confirmed by the pH-dependent activity of the catalysts and TMA$^+$ probe analysis. The first-principles calculations support the interpretation of the experimental observations and attribute the enhanced catalytic activity to a decrease in the adsorption energy of the intermediates, which correlates with the local changes in electronic charges of the adsorption sites induced by oxygen vacancies on Hm. Hence, this work provides microscopic insights into the OER reaction mechanism and represents an

important step forward towards the development of highly efficient and stable oxide-based catalysts to be used in next-generation energy devices.

Conflicts of interest

The authors declare no competing interests.

Acknowledgment

The authors are grateful to the Director CSIR-IMMT for his kind permission and encouragement for doing this work. BKJ acknowledges BRNS, Mumbai, India (No-2013/37P/67/BRNS), MNRE, New Delhi, India (No-102/87/2011-NT) and CSIR, New Delhi, India {YSP-02 (P-81-113), OLP-95} for the financial support. The Authors thank Prof. P. V. Satyam, and Prof. T. Som IoP Bhubaneswar for their constant guidance and support. The Authors thank Dr. A. Mitra, and Dr. R. Singh, IoP Bhubaneswar for characterization support. BPM acknowledge UGC, New Delhi for the fellowship. The authors thank HZDR computing cluster and PRACE (HLRS, Stuttgart, Germany) for the computational support. AVK acknowledges financial support from the DFG, project KR 4866/2-1.

References

1 S. Chu, A. Majumdar, E. G. S. Firmiano, M. A. L. Cordeiro, A. C. Rabelo, C. J. Dalmaschio, A. N. Pinheiro, E. C. Pereira and E. R. Leite, *Nature*, 2012, **488**, 294–303.

2 L. Li, Z. Wu, S. Yuan and X.-B. Zhang, *Energy Environ. Sci.*, 2014, **7**, 2101–2122.

3 J. S. Kim, B. Kim, H. Kim and K. Kang, *Advanced Energy Materials*, 2018, **8**, 1702774.

4 L. Han, S. Dong and E. Wang, *Advanced Materials*, 2016, **28**, 9266–9291.

5 M. K. Debe, *Nature*, 2012, **486**, 43.

6 F. Song, L. Bai, A. Moysiadou, S. Lee, C. Hu, L. Liardet and X. Hu, *Journal of the American Chemical Society*, 2018, **140**, 7748–7759.

7 N.-T. Suen, S.-F. Hung, Q. Quan, N. Zhang, Y.-J. Xu and H. M. Chen, *Chem. Soc. Rev.*, 2017, **46**, 337–365.

8 S. Siracusano, N. Van Dijk, E. Payne-Johnson, V. Baglio and A. S. Aricò, *Applied Catalysis B: Environmental*, 2015, **164**, 488–495.

9 P. Bhanja, B. Mohanty, A. K. Patra, S. Ghosh, B. K. Jena and A. Bhaumik, *ChemCatChem*, 2019, **11**, 583–592.

10 B. Mohanty, M. Ghorbani-Asl, S. Kretschmer, A. Ghosh, P. Guha, S. K. Panda, B. Jena, A. V Krasheninnikov and B. K. Jena, *ACS Catalysis*, 2018, **8**, 1683–1689.

11 S.-H. Ye, Z.-X. Shi, J.-X. Feng, Y.-X. Tong and G.-R. Li, *Angewandte Chemie International Edition*, 2018, **57**, 2672–2676.

12 S. Chen, Z. Kang, X. Zhang, J. Xie, H. Wang, W. Shao, X. Zheng, W. Yan, B. Pan and Y. Xie, *ACS Central Science*, 2017, **3**, 1221–1227.

13 S. Zhao, M. Li, M. Han, D. Xu, J. Yang, Y. Lin, N.-E. Shi, Y. Lu, R. Yang, B. Liu, Z. Dai and J. Bao, *Advanced Functional Materials*, 2018, **28**, 1706018.

14 A. Dutta, A. K. Samantara, S. K. Dutta, B. K. Jena and N. Pradhan, *ACS Energy Letters*, 2016, **1**, 169–174.

15 N. Dalai, B. Mohanty, A. Mitra and B. Jena, *ChemistrySelect*, 2019, **4**, 7791–7796.

16 S. Zhao, Y. Wang, J. Dong, C.-T. He, H. Yin, P. An, K. Zhao, X. Zhang, C. Gao, L. Zhang, J. Lv, J. Wang, J. Zhang, A. M. Khattak, N. A. Khan, Z. Wei, J. Zhang, S. Liu, H. Zhao and Z. Tang, *Nature Energy*, 2016, **1**, 16184.

17 Z. Cai, Y. Bi, E. Hu, W. Liu, N. Dwarica, Y. Tian, X. Li, Y. Kuang, Y. Li, X.-Q. Yang, H. Wang and X. Sun, *Advanced Energy Materials*, 2018, **8**, 1701694.

18 S. Kamila, B. Mohanty, A. K. Samantara, P. Guha, A. Ghosh, B. Jena, P. V. Satyam, B. K. Mishra and B. K. Jena, *Scientific Reports*, 2017, **7**, 1–13.

19 L. Xinran, W. Jilei, L. Qing, Z. Shasha, X. Yuxia, D. Pan, C. Changyun, Z. Jiyang, X. Huaiguo, X. Qiang and P. Huan, *Advanced Functional Materials*, **28**, 1800886.

20 B. Mohanty, B. K. Jena and S. Basu, *ACS Omega*, 2020, **5**, 1287–1295.

21 U. Kayal, B. Mohanty, P. Bhanja, S. Chatterjee, D. Chandra, M. Hara, B. Kumar Jena and A. Bhaumik, *Dalton Transactions*, 2019.

22 J. Bao, X. Zhang, B. Fan, J. Zhang, M. Zhou, W. Yang, X. Hu, H. Wang, B. Pan and Y. Xie, *Angewandte Chemie International Edition*, 2015, **54**, 7399–7404.

23 C. Tan, X. Cao, X.-J. Wu, Q. He, J. Yang, X. Zhang, C. Junze, W. Zhao, S. Han, G.-H. Nam, M. Sindoro and H. Zhang, *Recent Advances in Ultrathin Two-Dimensional Nanomaterials*, 2017, vol. 117.

24 A. Puthirath Balan, S. Radhakrishnan, S. K. Sinha, C. Woellner, L. Deng, C. de los Reyes, M. Banki, M. Paulose, R. Neupane, A. Apte, V. Kochat, R. Vajtai, A. R. Harutyunyan, C.-W. Chu, G. Costin, D. Galvao, A. A. Martí, P. A. van Aken, O. Varghese and P. M Ajayan, *Exfoliation of a non-van der Waals material from iron ore hematite*, 2018, vol. 13.

25 A. Puthirath Balan, S. Radhakrishnan, R. Kumar, R. Neupane, S. K. Sinha, L. Deng, C. A. de los Reyes, A. Apte, B. M. Rao, M. Paulose, R. Vajtai, C. W. Chu, G. Costin, A. A. Martí, O. K. Varghese, A. K. Singh, C. S. Tiwary, M. R. Anantharaman and P. M. Ajayan, *Chemistry of Materials*, 2018, **30**, 5923–5931.

26 K. Sivula, F. Le Formal and M. Grätzel, *ChemSusChem*, 2011, **4**, 432–449.

27 M. Marelli, A. Naldoni, A. Minguzzi, M. Allieta, T. Virgili, G. Scavia, S. Recchia, R. Psaro and V. Dal Santo, *ACS Applied Materials & Interfaces*, 2014, **6**, 11997–12004.

28 H. Wu, T. Yang, Y. Du, L. Shen and G. W. Ho, *Advanced Materials*, 2018, **30**, 1804341.

29 T. Ungár, *Scripta Materialia*, 2004, **51**, 777–781.

30 A. Banerjee, V. Aravindan, S. Bhatnagar, D. Mhamane, S. Madhavi and S. Ogale, *Superior lithium storage properties of α-Fe2O3 nano-assembled spindles*, 2013, vol. 2.

31 D. Bersani, P. P. Lottici and A. Montenero, *Journal of Raman Spectroscopy*, 1999, **30**, 355–360.

32 T. Zhai, S. Sun, X. Liu, C. Liang, G. Wang and H. Xia, *Advanced Materials*, 2018, **30**, 1706640.

33 M. Asnavandi, Y. Yin, Y. Li, C. Sun and C. Zhao, *ACS Energy Letters*, 2018, **3**, 1515–1520.

34 X. Lu, Y. Zeng, M. Yu, T. Zhai, C. Liang, S. Xie, M.-S. Balogun and Y. Tong, *Advanced Materials*, 2014, **26**, 3148–3155.

35 Y. Ling, G. Wang, J. Reddy, C. Wang, J. Z. Zhang and Y. Li, *Angewandte Chemie International Edition*, 2012, **51**, 4074–4079.

36 C. Zhu, C. Li, M. Zheng and J.-J. Delaunay, *ACS Applied Materials & Interfaces*, 2015, **7**, 22355–22363.

37 B. Zhang, X. Zheng, O. Voznyy, R. Comin, M. Bajdich, M. García-Melchor, L. Han, J. Xu, M. Liu, L. Zheng, F. P. García de Arquer, C. T. Dinh, F. Fan, M. Yuan, E. Yassitepe, N.

Chen, T. Regier, P. Liu, Y. Li, P. De Luna, A. Janmohamed, H. L. Xin, H. Yang, A. Vojvodic and E. H. Sargent, *Science*, 2016, **352**, 333 LP – 337.

38 M. W. Kanan, J. Yano, Y. Surendranath, M. Dincă, V. K. Yachandra and D. G. Nocera, *Journal of the American Chemical Society*, 2010, **132**, 13692–13701.

39 T. Wu, S. Sun, J. Song, S. Xi, Y. Du, B. Chen, W. A. Sasangka, H. Liao, C. L. Gan, G. G. Scherer, L. Zeng, H. Wang, H. Li, A. Grimaud and Z. J. Xu, *Nature Catalysis*, 2019.

40 Z.-F. Huang, J. Song, Y. Du, S. Xi, S. Dou, J. M. V. Nsanzimana, C. Wang, Z. J. Xu and X. Wang, *Nature Energy*, 2019, **4**, 329–338.

41 A. Grimaud, O. Diaz-Morales, B. Han, W. T. Hong, Y.-L. Lee, L. Giordano, K. A. Stoerzinger, M. T. M. Koper and Y. Shao-Horn, *Nat Chem*, 2017, **9**, 457–465.

42 C. Yang, O. Fontaine, J.-M. Tarascon and A. Grimaud, *Angewandte Chemie International Edition*, 2017, **56**, 8652–8656.

43 Y. Yao, S. Hu, W. Chen, Z.-Q. Huang, W. Wei, T. Yao, R. Liu, K. Zang, X. Wang, G. Wu, W. Yuan, T. Yuan, B. Zhu, W. Liu, Z. Li, D. He, Z. Xue, Y. Wang, X. Zheng, J. Dong, C.-R. Chang, Y. Chen, X. Hong, J. Luo, S. Wei, W.-X. Li, P. Strasser, Y. Wu and Y. Li, *Nature Catalysis*, 2019, **2**, 304–313.

44 I. V Chernyshova, M. F. Hochella Jr and A. S. Madden, *Physical Chemistry Chemical Physics*, 2007, **9**, 1736–1750.

45 R. Ovcharenko, E. Voloshina and J. Sauer, *Physical Chemistry Chemical Physics*, 2016, **18**, 25560–25568.

46 R. Zacharia, H. Ulbricht and T. Hertel, *Physical Review B*, 2004, **69**, 155406.

47 M. V. Ganduglia-Pirovano, A. Hofmann and J. Sauer, *Surface Science Reports*, 2007, **62**, 219–270.

48 M.-T. Nguyen, N. Seriani, S. Piccinin and R. Gebauer, *The Journal of Chemical Physics*, 2014, **140**, 64703.

49 N. Yatom, O. Neufeld and M. Caspary Toroker, *The Journal of Physical Chemistry C*, 2015, **119**, 24789–24795.

50 P. Liao, J. A. Keith and E. A. Carter, *Journal of the American Chemical Society*, 2012, **134**, 13296–13309.

51 T.-Y. Yang, H.-Y. Kang, U. Sim, Y.-J. Lee, J.-H. Lee, B. Koo, K. T. Nam and Y.-C. Joo, *Physical Chemistry Chemical Physics*, 2013, **15**, 2117–2124.

52 A. Hellman, B. Iandolo, B. Wickman, H. Grönbeck and J. Baltrusaitis, *Surface Science*, 2015, **640**, 45–49.